J_ID: JAP DOI: 10.1063/1.4800865 Date: 10-April-13 Stage: Page: 1 Total Pages: 7

JOURNAL OF APPLIED PHYSICS **113**, 000000 (2013)

Measurement of the elastic modulus of spider mite silk fibers using atomic force microscopy

Stephen D. Hudson,[1] Vladimir Zhurov,[2] Vojislava Grbić,[2] Miodrag Grbić,[2,3,a)] and Jeffrey L. Hutter[1,b)]

[1]*Department of Physics and Astronomy, The University of Western Ontario, London, Ontario N6A 3K7, Canada*

[2]*Department of Biology, The University of Western Ontario, London, Ontario N6A 5B7, Canada*

[3]*Instituto de Ciencias de la Vid y el Vino (ICVV) (CSIC, Universidad de La Rioja, Gobierno de La Rioja), 26006 Logroño, Spain*

(Received 13 November 2012; accepted 25 March 2013; published online xx xx xxxx)

Bio-nanomaterials are one of the fastest developing sectors of industry and technology. Spider silk, a highly attractive light-weight biomaterial, has high tensile strength and elasticity and is compatible with human tissues, allowing for many areas of application. In comparison to spider silk fibers with diameters of several micrometers, spider mite silk fibers have much smaller diameters of tens of nanometers, making conventional tensile testing methods impractical. To determine the mechanical properties of adult and larval *Tetranychus urticae* silk fibers, we have performed three-point bending tests with an atomic force microscope. We found that because of the small diameters of these fibers, axial tension—due to both the applied force and a pre-existing strain—has a significant effect on the fiber response, even in the small-deformation limit. As a result, the typical Euler-Bernoulli-Timoshenko theory cannot be applied. We therefore follow the approach of Heidelberg *et al*. to develop a mechanical model of the fiber response that accounts for bending, an initial tension in the fibers, and a tension due to elongation during testing. This model provides self-consistent results, allowing us to determine that adult and larval fibers have Young's moduli of 24 ± 3 GPa and 15 ± 3 GPa, respectively. Both adult and larval fibers have an estimated ultimate strength of 200–300 MPa and a toughness of order 9 MJ/m^3. We note that with increasing interest in the mechanical properties of very high aspect ratio nanomaterials, the influence of pre-existing tension must be considered in any measurements involving a bending test.
 [http://dx.doi.org/10.1063/1.4800865]

I. INTRODUCTION

Silk is an exceptionally strong natural material produced by spiders, silkworms, spider mites, and many other arthropods. Natural silkworm silk has long been exploited for textiles and, more recently, suture materials.[1–3] Silk also shows promise as a scaffold material for tissue repair and for generation of artificial tissue.[2–4] For this reason, there is great interest in characterizing the physical, chemical, and biological properties of silk and in producing synthetic silk fibers. Further, the properties of natural and artificial silk fibers vary considerably and depend on the silk proteins utilized, temperature, degree of hydration, and rate of deformation.[5]

Due to the length scales and magnitudes of forces involved, the atomic force microscope (AFM) is well suited to measuring the mechanical properties of nanofibers. In a typical approach, nanofibers are suspended across trenches and deformed laterally or vertically using the tip of an AFM probe, thus performing a three-point bending test. This technique has been used on a variety of materials including Au, Si, SiO_2, TiO_2, and ZnO nanowires,[6–10] carbon nanotubes,[11–13] and cellulose and assorted polymer nanofibers.[6,14–17] In some cases, elastic moduli that increased with decreasing nanofiber or nanowire diameter have been reported.[16,18] However, Heidelberg *et al*. showed that tensile stress, due to elongation of a deformed fiber, must be considered when the lateral displacement of the fiber is comparable to or larger than its radius.[8] In the cases of Si and ZnO nanowires, deformation-induced tensile stress could fully explain the apparent increase in modulus with decreasing nanowire diameter, and the moduli were found to equal those of the respective materials.[8,10]

Recently, the *Tetranychus urticae* two-spotted spider mite genome was fully sequenced, the proteins involved in silk production were identified, and the mechanical properties of naturally produced spider mite silk fibers were measured by atomic force microscopy, clearing the way for production and characterization of spider mite silks with genetically tailored mechanical properties.[19] To model the AFM data and determine the Young's modulus of the fibers, the model of Heidelberg *et al*. described above had to be modified to account for an initial axial tension, which is present even in the absence of applied forces from the AFM cantilever tip. Here, we present a detailed account of the AFM technique used and the derivation of the model employed to determine the Young's modulus from curves of fiber restoring force versus fiber deformation for fibers suspended over trenches.

a)Electronic mail: mgrbic@uwo.ca.
b)Author to whom correspondence should be addressed. Electronic mail: jhutter@uwo.ca.

J_ID: JAP DOI: 10.1063/1.4800865 Date: 10-April-13 Stage: Page: 2 Total Pages: 7

II. MATERIALS AND METHODS

The London strain of *T. urticae* (Koch) originates from a *T. urticae* population collected from the Vineland region (Ontario, Canada). The taxonomic status of the species was determined by the Agriculture Canada taxonomy division in Ottawa. Large-scale continuous propagation of the collected population was performed using controlled-environment insectaries at the Biotron facility at the University of Western Ontario. Animals were mass reared on bean plants in growth chambers at 27 °C with a 16:8 h (light:dark) photoperiod. The isofemale strain used for these experiments (London strain) underwent eight generations of sib-mating to maximize homozygosity.

Trenches were fabricated on silicon substrates by photolithography and reactive ion etching at the Western Nanofabrication Facility (London, Canada), using a custom-designed mask produced at the University of Alberta NanoFab facility (Edmonton, Canada). Silk fibers were deposited by allowing adult and larval *T. urticae* spider mites to walk on the silicon wafers for two to eight hours. Before performing measurements on the fibers, spider mites were removed from the silicon wafers with a fine brush. To reduce the time needed to find single fibers crossing trenches with the atomic force microscope, areas of spider mite activity were located by searching for bundles of fibers using an optical microscope (Olympus BX60).

Single silk fibers and bundles of several fibers were located by performing large-area contact AFM imaging on flat areas in the vicinity of the large fiber bundles located with the optical microscope. AFM measurements were made using a multimode atomic force microscope with a Nanoscope IIIa controller. NP-S silicon nitride cantilevers (Veeco Instruments) with nominal spring constants of 0.06 N/m and 0.35 N/m were used for measurements on larval and adult fibers, respectively. Actual spring constants of 0.083 ± 0.003 N/m and 0.347 ± 0.009 N/m were measured using the thermal noise method.[20–23] Measurements were performed at a temperature of approximately 32 °C, as measured at the sample position, and relative humidities of 14%–30%, although the relative humidity was typically less than 20%.

Contact imaging was used to track fibers to trenches, to verify that each fiber was firmly stuck to the plateau on each side of the trench, to measure the fiber lengths and diameters, and, in a few cases, to deliberately break fibers after acquiring force data. Fig. 1 shows a top view of a fiber spanning a trench acquired by contact-mode atomic force microscopy.

Once a fiber was located, mechanical testing was performed by measuring force curves, which record cantilever deflection versus the vertical position of the sample under the cantilever, acquired using vertical ramps of 1 μm at a rate of 4 Hz. Force-volume mode, which captures an array of such force curves, was used to acquire a 64×64 grid of such curves over an area encompassing the entire suspended portion of the fiber and parts of the plateaus beside the trench. For each force curve, data were acquired up to a predetermined maximum cantilever deflection, thus ensuring a consistent range of forces at each point in any given experiment.

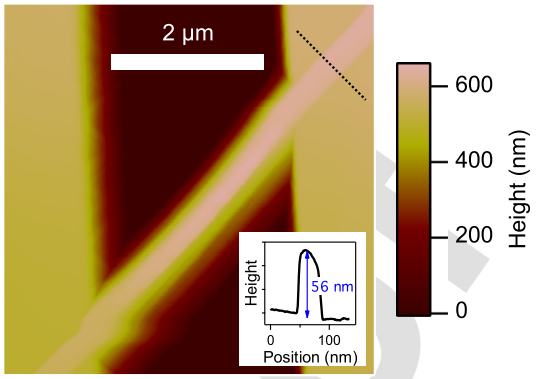

FIG. 1. 5.3 μm $\times$ 5.3 μm contact AFM image of a spider mite silk fiber suspended over a trench. The bottom of the trench has been moved off-scale in order to highlight the edges of the trench and the fiber. Note that the fiber appears much wider than its true diameter due to convolution with the pyramidal AFM tip. The diameter can be reliably measured from the vertical thickness of the portion of the fiber supported by the substrate. The inset shows a cross-section of the fiber measured at the location shown by the dotted line, with the measured diameter indicated.

An example force curve from near the center of the suspended portion of a fiber is shown in Fig. 2, along with a force curve acquired on the nearby substrate for reference.

Data were imported into Igor Pro (WaveMetrics) for analysis, and force curves on the fibers and the substrate were identified. The cantilever deflection supplied by the position-sensitive detector in the AFM is initially uncalibrated. Dividing each force curve by the magnitude of the mean slope of force curves acquired on the rigid substrate, where the cantilever deflection must equal the piezo displacement after contact is achieved, results in calibrated data, as shown in Fig. 2.

III. DATA ANALYSIS

The restoring force in principle results from a combination of bending, shear, and tensile stresses. However, when the aspect ratio (length divided by diameter) of a fiber is much greater than one, the shear stress is negligible in comparison to the bending stress.[24] As this is the case here, shear

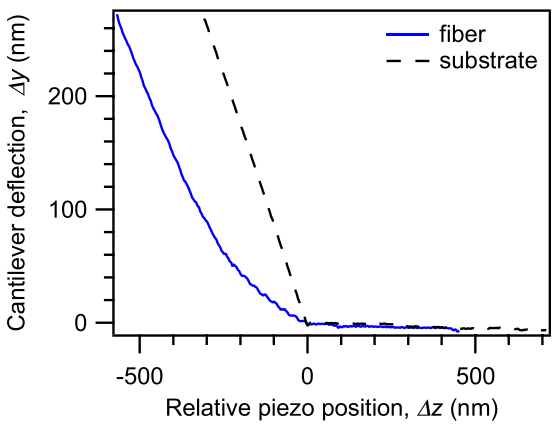

FIG. 2. AFM force curves obtained by pushing against a fiber (solid curve) and the rigid substrate (dashed curve). The sample approaches the cantilever with decreasing piezo position, with $\Delta z = 0$ chosen to be the point of contact. Note that Δy is measured relative to the mean deflection signal far from contact, where the cantilever deflection is expected to be zero.

J_ID: JAP DOI: 10.1063/1.4800865 Date: 10-April-13 Stage: Page: 3 Total Pages: 7

stress is not considered in the analysis below. Further, the radius of curvature everywhere on the fiber is assumed to be large relative to the fiber diameter, which is satisfied for fiber displacements much smaller than the length of the fiber, as is the case here. To develop the theory, we further assume that the material is linearly elastic for axial strains. As we will see later, this assumption is valid for small deformations and sufficient for determining the Young's modulus. Finally, to simplify the analysis, we only consider the case when the cantilever tip pushes at the center of the fiber.

In many AFM studies of other fibers, force curves on the fiber are linear, and fiber deflection is attributed to bending and/or shear.[6,14–17] In the pure bending case, the equilibrium displacement, $\delta(x)$, of a beam or fiber deflected by a force of magnitude F_c applied at its center may be determined as a function of the position x along the fiber from

$$EI\frac{d^3\delta(x)}{dx^3} = -\frac{F_c}{2}, \tag{1}$$

where E is the Young's modulus of the fiber and I its area moment of inertia.[25] With clamped boundary conditions and noting that the solution must be symmetric about the center, $x = L_0/2$, the solution must satisfy $\delta(0) = 0$ and $\delta'(0) = \delta'(L_0/2) = 0$, where L_0 is the length of fiber between the clamped boundaries. The solution, after isolation of the magnitude of the force at the center, F_c, is

$$F_c = \frac{192EI}{L_0^3}\delta_c, \tag{2}$$

where $\delta_c = \delta(L/2)$ is the displacement of the fiber at its center.[25] Note that Eq. (2) predicts a linear relation between force and displacement.

In our case, we find nonlinear force curves, indicating a need to consider tensile stress. When an axial tension of magnitude T is present, the vertical components of the tension in an infinitesimal element of the fiber act like shear forces on the ends of the element, requiring modification of Eq. (1). In the small-deflection limit where the slope of the fiber remains small, the vertical component of the tension at position x is $Td\delta(x)/dx$, and the new equation for equilibrium of the fiber is[25]

$$EI\frac{d^3\delta(x)}{dx^3} = -\frac{F_c}{2} + T\frac{d\delta(x)}{dx}. \tag{3}$$

Assuming linear elasticity, the tension due to stretching the fiber from an initial length L_0 to a stretched length L is given by

$$T_s = \sigma A = EA\epsilon = EA\frac{L - L_0}{L_0}, \tag{4}$$

where σ is the axial stress in the fiber, A its cross-sectional area, and ϵ is the axial strain in the fiber. The stretched length L can be calculated from the fiber profile $\delta(x)$ as[25]

$$L = L_0 + \int_0^{L_0/2}\left(\frac{d\delta}{dx}\right)^2 dx. \tag{5}$$

Heidelberg *et al.*[8] solved Eq. (3) for clamped boundary conditions and the tension given by Eqs. (4) and (5) to obtain the relationship

$$F_c = \frac{192EI}{L_0^3}f(\alpha)\delta_c, \tag{6}$$

where

$$f(\alpha) = \alpha\left[48 - \frac{192\tanh(\sqrt{\alpha}/4)}{\sqrt{\alpha}}\right]^{-1}, \tag{7}$$

and the dimensionless parameter α is defined by

$$\alpha = \frac{TL_0^2}{EI}, \tag{8}$$

and $T = T_s$ is the magnitude of the tension due to stretching of the fiber. Note that T, and hence α, varies with the applied force. Heidelberg *et al.* used their solution for the fiber shape to relate α and δ_c through the transcendental equation

$$\frac{\alpha\cosh^2(\sqrt{\alpha}/4)}{2+\cosh(\sqrt{\alpha}/2)-6\frac{\sinh(\sqrt{\alpha}/2)}{\sqrt{\alpha}}}\left(1-4\frac{\tanh(\sqrt{\alpha}/4)}{\sqrt{\alpha}}\right)^2 = \frac{A}{I}\delta_c^2. \tag{9}$$

They found that the tensile stress due to elongation becomes significant when the lateral fiber displacement is comparable to or larger than the fiber radius and applied Eqs. (6) through (9) to AFM three-point bending tests of nanowires. The function $f(\alpha)$, which is greater than or equal to one, is the factor

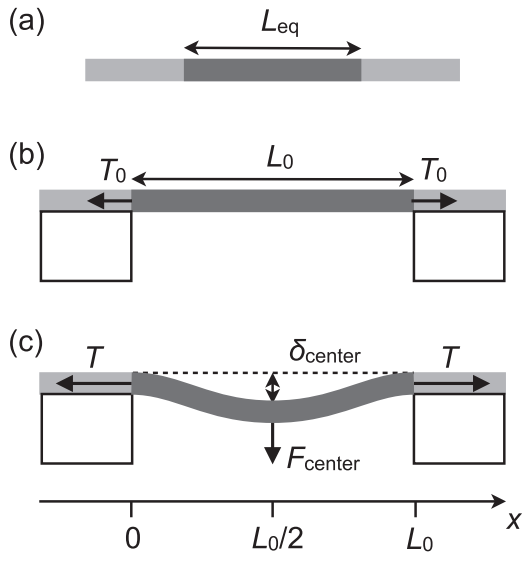

FIG. 3. Diagram of the segment of fiber under analysis (a) before clamping and without initial tension, (b) after application of initial tension and clamping to grating but before contact with the AFM cantilever tip, and (c) after contact with the AFM cantilever tip. The fiber is shown in light grey, and the segment under analysis in dark grey. L_{eq} is the equilibrium length of the section of fiber stretched by an initial tension T_0 to the distance L_0 between clamping points. When the fiber is deflected by an amount δ_c by a force F_c applied at its midpoint $x = L_0/2$, the total axial tension increases to $T = T_0 + T_s$, the sum of the initial tension and the tension due to elongation of the fiber.

by which tensile stress increases the fiber's resistance to deformation relative to Eq. (2), which considers only bending stress. An analytic expression for α cannot be found from Eq. (9) but may be solved numerically (our choice in this work) or approximated analytically using a Padé approximant.[8]

We extend the model of Heidelberg *et al.* by considering the case in which a constant initial tension T_0 is applied to the fiber, as shown in Fig. 3. Since the suspended fiber segment of length L_0 is under tension, its relaxed equilibrium length, L_{eq}, is less than L_0, as indicated in Figs. 3(a) and 3(b). Equation (3) then defines the equilibrium shape of the fiber with $T = T_0 + T_s$ in the presence of a lateral force F_c applied to its center as shown in Fig. 3(c). With assistance from Maple (Maplesoft, Waterloo, Canada), we find that for the case of a clamped fiber of suspended length L_0 subjected to a lateral force F_c applied at its center, the displacement of the fiber between $x = 0$ and $x = L_0/2$ is

$$\delta(x) = \frac{F_c}{2T}\left[x - \frac{L_0}{\sqrt{\alpha}}\frac{\sinh[\sqrt{\alpha}(x/L_0 - 1/4)] + \sinh(\sqrt{\alpha}/4)}{\cosh(\sqrt{\alpha}/4)}\right]. \tag{10}$$

Restoring force versus deformation can still be expressed using Eqs. (6)–(8). However, introducing the additional tension T_0 changes the relationship between α and δ_c as is found below.

Assuming the fiber remains in the linear limit, the additional tension due to stretching, relative to the relaxed equilibrium length, is given by

$$T_s = EA\frac{L - L_0}{L_{eq}} = \frac{EA}{L_{eq}}\int_0^{L_0/2}\left(\frac{d\delta}{dx}\right)^2 dx. \tag{11}$$

Substitution of Eq. (10) into Eq. (11) yields

$$\frac{T_s}{T}\frac{L_{eq}}{L_0}\left[\frac{\alpha\cosh^2(\sqrt{\alpha}/4)}{2 + \cosh(\sqrt{\alpha}/2) - 6\dfrac{\sinh(\sqrt{\alpha}/2)}{\sqrt{\alpha}}}\left(1 - 4\frac{\tanh(\sqrt{\alpha}/4)}{\sqrt{\alpha}}\right)^2\right] = \frac{A}{I}\delta_c^2. \tag{12}$$

By definition

$$T_0 = EA\frac{L_0 - L_{eq}}{L_{eq}},$$

so

$$L_{eq} = L_0\left(\frac{EA}{T_0 + EA}\right). \tag{13}$$

Using Eqs. (8) and (13) and $T_s = T - T_0$, Eq. (12) may be written as

$$\left(1 - \frac{L_0^2 T_0}{\alpha EI}\right)\left(\frac{EA}{T_0 + EA}\right) \times \left[\frac{\alpha\cosh^2(\sqrt{\alpha}/4)}{2 + \cosh(\sqrt{\alpha}/2) - 6\dfrac{\sinh(\sqrt{\alpha}/2)}{\sqrt{\alpha}}}\left(1 - 4\frac{\tanh(\sqrt{\alpha}/4)}{\sqrt{\alpha}}\right)^2\right] = \frac{A}{I}\delta_c^2, \tag{14}$$

providing a relationship between α and δ_c different from that of Eq. (9) in the previous model. Note that when $T_0 = 0$, Eq. (9) is recovered.

IV. RESULTS AND DISCUSSION

To facilitate the use of Eqs. (6), (7), and (14) to model our mechanical data, force curves were converted to force-versus-displacement data by manually determining the contact point and calculating the fiber displacement as $\delta = \Delta y + \Delta z$ and the corresponding restoring force as $k\Delta y$ for all positions in which the tip and sample are in contact—i.e., for all points with $\Delta z < 0$. Fibers were assumed to have circular cross-sections, for which $I = \pi d^4/64$ and $A = \pi d^2/4$, where d is the diameter of the fiber.

Our system of Eqs. (6), (7), and (14) was fit to force-versus-displacement curves with only the Young's modulus, E, and the initial tension, T_0, as free parameters. Examples of force-versus-displacement curves with relatively small and large initial tensions are shown in Fig. 4 along with corresponding least-squares fits to our model. For comparison, fits to both the pure bending Euler-Bernoulli model and the model of Heidelberg *et al.* including bending and stretching but without an initial tension are also shown. The range of the pure bending fits were restricted to δ_c less than 50 nm in an attempt to fit only the linear regions of the curves. In the case of high initial tension, fits of the other two models were restricted to δ_c less than 150 nm to fit only the region of linear elastic deformation.

In the examples shown in Fig. 4, the Euler-Bernoulli model yields moduli of 580 ± 20 and 167 ± 2 GPa, while the model of Heidelberg *et al.* yields moduli of 32 ± 0.2 and 46.7 ± 0.9 GPa, for examples (a) and (b), respectively. These models thus provide inconsistent results despite the restriction to the low-deflection limit and, as we will see, significantly overestimate the modulus of the silk.

As shown by Eqs. (6)–(8), an initial tension results in α greater than zero, $f(\alpha)$ greater than one, and an increased slope of F_c versus δ_c. In the case of a fiber with circular cross-section, the initial value of α, α_0, as a function of the initial strain, ϵ_0, is given by

J_ID: JAP DOI: 10.1063/1.4800865 Date: 10-April-13 Stage: Page: 5 Total Pages: 7

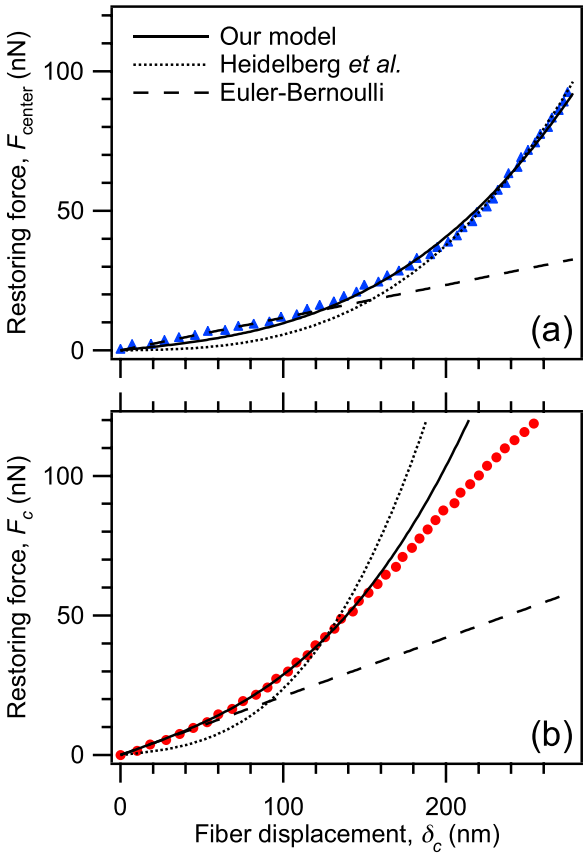

FIG. 4. Experimental force versus displacement curves for single silk fibers with (a) relatively low and (b) relatively high initial tensions. For clarity, two-thirds of the data points have been omitted. Fits to our model, which accounts for bending, stretching, and an initial tension, are shown with solid curves. For comparison, fits to the pure bending and bending plus stretching models are shown for each dataset with dashed and dotted curves, respectively. The range of the pure bending fits were restricted to δ_c less than 50 nm. In the case of high initial tension (b), fits to the other two models were restricted to less than 150 nm.

$$\alpha_0 = 16\left(\frac{L_0}{d}\right)^2 \epsilon_0 = 16\frac{T_0}{EA}\left(\frac{L_0}{d}\right)^2, \quad (15)$$

where L_0/d is the aspect ratio of the fiber. This relationship demonstrates that for fibers with high aspect ratios such as those studied here, the initial value of α, and hence even the *initial* slope of force-versus-displacement curves, is strongly influenced by any initial strain of the fibers. With the inclusion of the initial tension T_0 in the model presented here, moduli of 25.4 ± 0.3 and 22.9 ± 0.3 GPa and initial tensions of 46 ± 2 and 155 ± 2 nN are obtained, for examples (a) and (b) in Fig. 4, respectively. These initial tensions correspond to initial strains of 0.22% and 0.30%, respectively.

Though the model was developed for loads applied at the center of the fiber, we find that the moduli given by the model are fairly constant over at least the middle 20% of force curves (approximating x as $L_0/2$ for each), as shown in Fig. 5. We therefore average the values obtained from force curves located within $\pm 10\%$ of the center of the fiber. The Young's moduli and initial tensions of fibers and fiber bundles, obtained using the method described above for samples prepared with a mixture of adults and larvae, adults only, and larvae only, are recorded in Table I. The

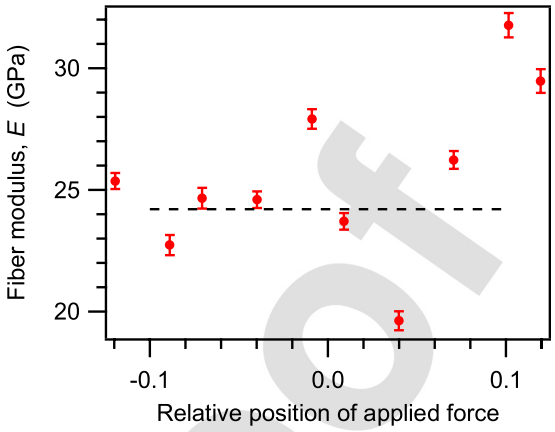

FIG. 5. Young's modulus, obtained from fitting individual force curves obtained from a single fiber, displayed versus position of the force curve relative to the center of the fiber as a fraction of fiber length. Error bars represent the statistical uncertainty of the individual curve fits and do not consider the effects of position along the fiber nor of the uncertainty in parameters such as the fiber radius. The reported modulus of the fiber was determined by averaging the middle 20% of measurements, the result of which is indicated by the dashed line.

diameters suggest three cases in which a measurement was made on a small bundle with a few fibers and four cases in which a measurement was made on a larger fiber bundle with a height above the substrate greater than 100 nm. In a few cases, consecutive measurements were made to test the repeatability of the experiments. Averages of the results for repeated measurements are recorded. Also included is the average value of the factor $f(\alpha_0)$, which characterizes the enhancement of the apparent bending rigidity of the fiber due to the pre-existing tension, for each fiber.

TABLE I. Silk fiber lengths, diameters, moduli, and initial tensions for samples prepared with adults and larvae, adults only, and larvae only.

Sample type	Fiber	Location	L (μm)	d (nm)	E (GPa)	T_0 (nN)	$f(\alpha_0)$
Mixed	1	i	4.2	57	27.4 ± 7.6	486 ± 40	15
		i	4.1	59	27.6 ± 4.1	205 ± 10	6.0
		iii	3.9	51	40.6 ± 3.3	80 ± 12	3.2
		iv	4.1	59	15.7 ± 0.7	255 ± 5	12
	2	i	6.8	75[a]	39.9 ± 5.8	628 ± 39	12
	3	i	4.2	170[b]	26.5 ± 1.0	201 ± 86	1.1
		i	4.4	190[b]	19.3 ± 2.3	0.7 ± 0.5	1.0
		iii	4.4	200[b]	25.3 ± 0.9	510 ± 100	1.1
	4	i	18	92[a]	25.4 ± 4.3	621 ± 28	51
		ii[c]	16	78[a]	31.6 ± 2.9	366 ± 21	38
Adult	5	i	3.8	33	24.2 ± 1.0	9 ± 4	3.3
	6	i	3.4	108[b]	26.0 ± 1.2	231 ± 35	1.4
	7	i	4.4	65	15.2 ± 1.1	91 ± 14	4.2
		ii	4.4	54	20.5 ± 0.5	79 ± 6	5.3
	8	ii[d]	4.0	54	19.6 ± 0.3	238 ± 2	12
Larval	9	i	3.6	23	20.3 ± 4.0	14 ± 4	16
	10	i[c]	6.0	25	9.55 ± 0.48	32 ± 2	140
	11	i[e]	4.3	22	15.16 ± 0.56	90 ± 2	210

[a]Likely multiple fibers.
[b]Large fiber bundle.
[c]Average of four consecutive measurements.
[d]Average of three consecutive measurements.
[e]Average of two consecutive measurements.

J_ID: JAP DOI: 10.1063/1.4800865 Date: 10-April-13 Stage: Page: 6 Total Pages: 7

From contact imaging on the substrate, adult fibers were found to have a diameter of approximately 55 nm. Several of the fibers from the mixed adult and larval samples have diameters matching those from the adult only samples. We therefore classify fibers 1, 5, 7, and 8 from Table I as individual adult fibers. Their average diameter is 54 ± 3 nm. The larval fibers, fibers 9, 10, and 11, have a significantly smaller average diameter of 23.3 ± 0.9 nm. The remaining fibers have diameters greater than 70 nm and are assumed to be bundles of fibers. The initial tensions of the strands vary from negligibly small to hundreds of nanoNewtons. These tensions may arise from mites pulling on the silk as they lay it down or from shrinkage of the silk after it has been deposited. Despite the variation in T_0, the values of Young's modulus show little variation. The average of the moduli of the adult fibers is 24 ± 3 GPa, and the average of the moduli of the larval fibers is 15 ± 3 GPa.

In cases of high initial tension, such as that shown in Fig. 4(b), the shapes of the force curves suggest deformation beyond the elastic limit. To explore the nonlinear elastic properties of our fibers, we estimated the tensile stress versus engineering tensile strain as follows. Neglecting the variation in strain due to curvature of the fibers, the uniform tensile strain for each point along the F_c versus δ_c curves is given by

$$\epsilon = \frac{L - L_{eq}}{L_{eq}},$$

where L_{eq} is provided by the fitting results through Eq. (13) and L is determined from Eq. (5) and the derivative of Eq. (10). Note that we assume that even if the elastic limit is exceeded, the fiber retains the shape predicted by the model of Heidelberg *et al*. Fiber restoring force was converted to engineering tensile stress from

$$\sigma = \frac{T}{A},$$

by determining T for each pair of experimental force-displacement values through Eqs. (6)–(8) and (14), with the modulus E (but not the initial tension T_0) allowed to vary with strain.

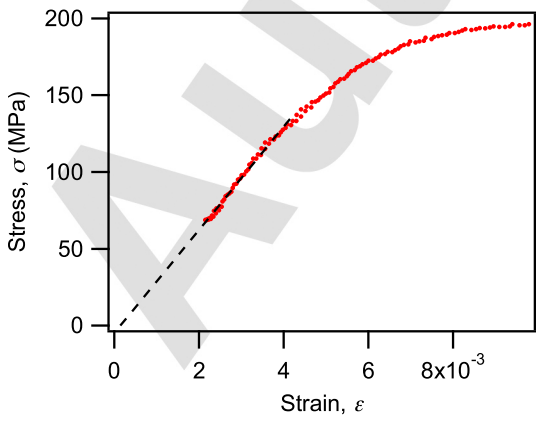

FIG. 6. An example plot of tensile stress versus tensile strain. Experimental stress-strain data are shown with circles. The dashed curve shows a linear fit to the linear region of experimental data (in this case, for $\epsilon < 4 \times 19^{-3}$) that has been extrapolated back to zero strain.

TABLE II. Comparison of the elastic modulus, tensile strength, breaking strain, and toughness of adult spider mite, spider, and silkworm silks. The spider and silkworm data are from Elices *et al*.[26]

Silk	Elastic Modulus (GPa)	Tensile Strength (GPa)	Breaking Strain (%)	Toughness (MJ/m^3)
Spider mite[a]	24 ± 3	~0.2–0.3	~4	~9
Spider[b]	1–10	1.8	30	≥ 130
Silk worm[c]	5	0.6	12	≥ 50

[a]Tetranychus urticae.
[b]Nephila clavipes.
[c]Bombyx mori.

An example plot of the tensile stress versus tensile strain curves thus obtained is shown in Fig. 6. The initial tension in the fiber studied is responsible for the data beginning above zero strain. The extrapolated linear fit nearly passes through the point of zero stress at zero strain, demonstrating that it is reasonable to assume that the material exhibits linear elastic behavior at low strains.

An estimate of the ultimate tensile strength could be made in cases where large enough forces were applied that the stress became flat with increasing strain. Both adult and larval fibers had ultimate tensile strengths of approximately 200–300 MPa, typically reached at 1%–1.5% strain. To obtain an estimate of the toughness, several fibers were broken by repeating contact imaging with gradually increasing imaging force. An estimate of the lateral deformation of the center of a fiber was made from the last contact image obtained before the fiber broke, allowing us to estimate a maximum strain of ~4%. If we assume that the stress increases linearly from 0 to 250 MPa between 0% and 1% strain and remains constant thereafter until the fiber breaks at 4% strain, we can make an order-of-magnitude estimate of 9 MJ/m^3 for the toughness.

The elastic modulus, tensile strength, breaking strain, and toughness of the spider mite silk fibers is compared to those of the *Nephila clavipes* spider and the *Bombyx mori* silk worm silks in Table II. The spider mite silk has a higher modulus than the spider and silk worm silks. However, the tensile strength, breaking strain, and toughness of the spider mite silk are lower than those of the spider and silk worm silks. The low toughness of spider mite silk relative to that of spider silk is perhaps not surprising, given that the former did not evolve to capture large prey. Nevertheless, spider mite silk possesses a larger elastic modulus than spider silk and, unlike other silks, is a true natural nanomaterial, which may permit applications impractical for other silks.

V. CONCLUSION

In summary, the mechanical properties of adult and larval spider mite silk nanofibers deposited onto silicon gratings were determined by measuring fiber restoring force versus vertical displacement with an atomic force microscope and modeling the fibers as clamped beams made of a

linear elastic material. Since the fiber displacements were greater than their radii, tensile stresses had to be considered. However, the model of Heidelberg *et al*. was insufficient for our data, and an initial tension in the fibers had to be included. We have presented a model for determining the Young's modulus of suspended nanofibers with clamped boundaries that accounts for bending stress, tensile stress due to elongation during deformation, and tensile stress due to an initial tension. We note that the latter stress changes the *initial* slope of the force-versus-displacement curves and so must be considered even in the limiting case of small displacements. Despite force versus displacement curves ranging from nearly linear to highly nonlinear, our model provides consistent measurements of the elastic modulus of spider mite silk fibers. To our knowledge, this is the first study to incorporate axial tension due both to the applied force and pre-existing tension in the analysis of nanofiber properties. We recommend that such contributions to the axial tension be considered in cases whenever the initial tension T_0 results in a value of $f(\alpha_0)$ as given by Eqs. (7) and (15) that is significantly greater than one.

ACKNOWLEDGMENTS

The authors thank NSERC (Canada) for operation funding of this project and the Canada Foundation for Innovation and Ontario Innovation Trust for the AFM infrastructure used. The authors also thank Mark Gooyers for designing the silicon gratings. M.G. and V.G acknowledge support from NSERC Strategic Grant STPGP 322206-05, Ontario Research Fund–Global Leadership in Genomics and Life Sciences GL2-01-035, and Genome Canada and the Ontario Genomics Institute grant (OGI-046).

[1]*Silk Polymers: Materials Science and Biotechnology*, edited by D. Kaplan, W. W. Adams, B. Farmer, and C. Viney (American Chemical Society, 1994).
[2]G. H. Altman, F. Diaz, C. Jakuba, T. Calabro, R. L. Horan, J. Chen, H. Lu, J. Richmond, and D. L. Kaplan, Biomaterials **24**, 401 (2003).
[3]A. C. MacIntosh, V. R. Kearns, A. Crawford, and P. V. Hatton, J. Tissue Eng. Regener. Med. **2**, 71 (2008).
[4]S. Hofmann, S. Knecht, R. Langer, D. L. Kaplan, G. Vunjak-Novakovic, H. P. Merkle, and L. Meinel, Tissue Eng. **12**, 2729 (2006).
[5]J. M. Gosline, M. E. DeMont, and M. W. Denny, Endeavour **10**, 37 (1986).
[6]S.-H. Lee, C. Tekmen, and W. M. Sigmund, Mater. Sci. Eng., A **398**, 77 (2005).
[7]B. Wu, A. Heidelberg, and J. J. Boland, Nat. Mater. **4**, 525 (2005).
[8]A. Heidelberg, L. T. Ngo, B. Wu, M. A. Phillips, S. Sharma, T. I. Kamins, J. E. Sader, and J. J. Boland, Nano Lett. **6**, 1101 (2006).
[9]H. Ni, X. Li, and H. Gao, Appl. Phys. Lett. **88**, 043108 (2006).
[10]B. Wen, J. E. Sader, and J. J. Boland, Phys. Rev. Lett. **101**, 175502 (2008).
[11]J.-P. Salvetat, J.-M. Bonard, N. H. Thomson, A. J. Kulik, L. Forró, W. Benoit, and L. Zuppiroli, Appl. Phys. A **69**, 255 (1999).
[12]G.-T. Kim, G. Gu, U. Waizmann, and S. Roth, Appl. Phys. Lett. **80**, 1815 (2002).
[13]G. Guhados, W. Wan, X. Sun, and J. L. Hutter, J. Appl. Phys. **101**, 033514 (2007).
[14]E. P. S. Tan and C. T. Lim, Appl. Phys. Lett. **84**, 1603 (2004).
[15]G. Guhados, W. Wan, and J. L. Hutter, Langmuir **21**, 6642 (2005).
[16]M. K. Shin, S. I. Kim, and S. J. Kim, Appl. Phys. Lett. **89**, 231929 (2006).
[17]S. Iwamoto, W. Kai, A. Isogai, and T. Iwata, Biomacromolecules **10**, 2571 (2009).
[18]C. Q. Chen, Y. Shi, Y. S. Zhang, J. Zhu, and Y. J. Yan, Phys. Rev. Lett. **96**, 075505 (2006).
[19]M. Grbić, T. Van Leeuwen, R. M. Clark, S. Rombauts, P. Rouzé, V. Grbić, E. J. Osborne, W. Dermauw, P. C. T. Ngoc, F. Ortego, P. Hernández-Crespo, I. Diaz, M. Martinez, M. Navajas, É. Sucena, S. Magalhães, L. Nagy, R. Pace, S. Djuranović, G. Smagghe, M. Iga, O. Christiaens, J. A. Veenstra, J. Ewer, R. M. Villalobos, J. L. Hutter, S. D. Hudson, M. Velez, S. V. Yi, J. Zeng, A. Pires-daSilva, F. Roch, M. Cazaux, M. Navarro, V. Zhurov, G. Acevedo, A. Bjelica, J. A. Fawcett, E. Bonnet, C. Martens, G. Baele, L. Wissler, A. Sanchez-Rodriguez, L. Tirry, C. Blais, K. Demeestere, S. R. Henz, T. R. Gregory, J. Mathieu, L. Verdon, L. Farinelli, J. Schmutz, E. Lindquist, R. Feyereisen, and Y. Van de Peer, Nature (London) **479**, 487 (2011).
[20]J. L. Hutter and J. Bechhoefer, Rev. Sci. Instrum. **64**, 1868 (1993).
[21]H.-J. Butt and M. Jaschke, Nanotechnology **6**, 1 (1995).
[22]D. A. Walters, J. P. Cleveland, N. H. Thomson, P. K. Hansma, M. A. Wendman, G. Gurley, and V. Elings, Rev. Sci. Instrum. **67**, 3583 (1996).
[23]J. L. Hutter, Langmuir **21**, 2630 (2005).
[24]S. P. Timoshenko, Philos. Mag. **41**, 744 (1921).
[25]L. D. Landau and E. M. Lifshitz, *Theory of Elasticity*, 2nd ed. (Pergamon Press, 1970).
[26]M. Elices, J. Pérez-Rigueiro, G. R. Plaza, and G. V. Guinea, J. Mater. **57**, 60 (2005).